



## SOIR/VEx observations of water vapor at the terminator in the Venus mesosphere

S. Chamberlain<sup>a</sup>, A. Mahieux<sup>a,b,c,\*</sup>, S. Robert<sup>a</sup>, A. Piccialli<sup>a</sup>, L. Trompet<sup>a</sup>, A.C. Vandaele<sup>a</sup>, V. Wilquet<sup>a</sup>

<sup>a</sup> Royal Belgian Institute for Space Aeronomy, Brussels, Belgium

<sup>b</sup> Fonds National de la Recherche Scientifique, Brussels, Belgium

<sup>c</sup> The University of Texas at Austin, Austin, TX, United States of America

### ABSTRACT

The Solar Occultation in the InfraRed (SOIR) instrument onboard Venus Express sounded the Venus mesosphere and lower thermosphere using solar occultation geometry between April 2006 and December 2014. The observations were all taken at the terminator. This paper reports on the water vapor vertical distribution above the clouds and geo-temporal variations, observed across the whole Venus Express mission. Water vapor profiles are sampled between 80 and 125 km from both the morning and evening side of the terminator. Calculations of the water vapor volume mixing ratio agree with those from previous studies, having an average atmospheric profile that varies between 0.56 ppmv and 2.45 ppmv. No significant variations were observed in observations taken between the morning and evening terminator. Short term variations of several Earth days dominate the data set, varying by up to a factor 18 over a 24 h period, from  $\sim 10$  ppmv to  $\sim 0.55$  ppmv at an altitude of  $\sim 111$  km. Similar to previous trace gas observations by SOIR (HCl, HF and SO<sub>2</sub>), no significant spatial or long term trends are observed.

### 1. Introduction

Water vapor is an important minor constituent in the Venus mesosphere as it can be used as a tracer to characterize both atmospheric dynamics and photochemical cycles.

At mesospheric altitudes, H<sub>2</sub>O dissociates and forms H, OH and HO<sub>2</sub>. These species are highly reactive and interact with other gaseous molecules. Photochemical models show that the mesospheric SO<sub>2</sub> abundance controls the H<sub>2</sub>O distribution, to which it is anti-correlated (Mills et al., 2007; Parkinson et al., 2015b; Zhang et al., 2012; Zhang et al., 2010). Krasnopolsky (2012) and Parkinson et al. (2015a) photochemical models indicate that chemistry at  $\sim 40$  km might also control the abundance of H<sub>2</sub>O above 70 km through eddy diffusion and complex chemistry surrounding the formation and condensation of H<sub>2</sub>SO<sub>4</sub>. In a review of these works Marcq et al. (2018) suggests that the H<sub>2</sub>O abundance could display a chemical bifurcation. As the H<sub>2</sub>O value falls below a critical value at  $\sim 40$  km, there appears to be a sudden fall off of H<sub>2</sub>O above 65 km due to the complete sequestration of H<sub>2</sub>O. Whilst SO<sub>2</sub> displays huge temporal variability above the clouds, which is still largely unexplained (Vandaele et al., 2017a; Vandaele et al., 2017b), variations in H<sub>2</sub>O at these altitudes have been difficult to detect by instruments prior to Venus Express (VEx). Unlike SO<sub>2</sub>, H<sub>2</sub>O variations are inferred from HDO observations, to be  $<10\%$  its mean value ( $<100$  ppbv

(Encrenaz et al., 2016).

Atmospheric haze, interpreted as sulfuric acid in water solution, has been observed above the clouds from 70 km to as high as 100 km by the SOIR instrument, where it nears the instrument detection limit, and displays both long and short term variability (Luginin et al., 2016; Wilquet et al., 2012). We note that temperature variations of 10–15 K at these altitudes could cause condensation/evaporation processes of the atmospheric haze, which should be identifiable in the water vapor abundance (Gurwell et al., 2007; Mills, 1999). Detached mesospheric haze layers (primarily between 80 and 90 km) were detected using SPICAV IR (Luginin et al., 2018). These haze layers are presumed to form through condensation of water on droplets of sulfuric acid water solution and correspond to altitudes of H<sub>2</sub>O gas depletion.

Dynamical and chemical interpretations of the observed region are complex for multiple reasons. The mesosphere is known to be a dynamical transition region between the strong global zonal circulation of the cloud layer in the lower atmosphere to the subsolar to antisolar (SS-AS) flow higher in the thermosphere. The occultation technique used by SOIR also restricts the observations to the terminator, where photolysis driven dynamical and chemical cycles are weaker due to the large solar zenith angle. Studying the spatial and temporal distribution, profile and abundance of water vapor at the terminator in the mesosphere is therefore critical to the understanding and interpretation of

\* Corresponding author at: The University of Texas at Austin, Austin, TX, United States of America.

E-mail address: [arnaud.mahieux@aeronomie.be](mailto:arnaud.mahieux@aeronomie.be) (A. Mahieux).

<https://doi.org/10.1016/j.icarus.2020.113819>

Received 27 August 2019; Received in revised form 31 March 2020; Accepted 7 April 2020

Available online 25 April 2020

0019-1035/© 2020 The Authors.

Published by Elsevier Inc.

This is an open access article under the CC BY-NC-ND license

(<http://creativecommons.org/licenses/by-nc-nd/4.0/>).

**Table 1**  
Previous observations of H<sub>2</sub>O in the Venus mesosphere.

Observation type	Year of observation	Altitude sensitivity range	H <sub>2</sub> O VMR (ppmv)	Citation
mm	1991	>65 km	3.5 (±2)	(Encrenaz et al., 1991)
mm	1991	>65 km	1 (+1, -0.5)	(Encrenaz et al., 1995)
mm	1993	>65 km	7 (+5, -4)	(Encrenaz et al., 1995)
mm	1998–2004	65–100 km	0.1–3.5	(Sandor and Clancy, 2005)
Sub-mm	2002–2004	65–105 km	<0.03–4.5 (±1.5)	(Gurwell et al., 2007)
Thermal Infrared	2012–2016	64–85 km	1–1.5	(Encrenaz et al., 2012a; Encrenaz et al., 2016; Encrenaz et al., 2013)
Near Infrared (SOIR)	Dec2006–Jan2007	70–110 km	0.4–1.3	(Bertaux et al., 2007)
Near Infrared (SOIR)	Apr2006–Aug2007	70–110 km	1.16 (±0.24)	(Fedorova et al., 2008)

both physical and chemical processes that occur.

Water vapor studies of the Venus mesosphere were not possible prior to the development of millimetre and submillimetre astronomy (Encrenaz et al., 2016; Encrenaz et al., 2013; Encrenaz et al., 2012b; Encrenaz et al., 1995; Encrenaz et al., 1991; Gurwell et al., 2007; Piccialli et al., 2017; Sandor and Clancy, 2005). Early ground based studies are predominantly disk averaged and sensitive to the altitude range of 65 km–100 km, however more recent observations have achieved a spatial resolution of 1–1.5 arcsec (for disk sizes of 12–33 arcsec) and are sensitive to the lower mesosphere, 60–80 km (Encrenaz et al., 2016; Encrenaz et al., 2013; Encrenaz et al., 2012b).

Sandor and Clancy (Sandor and Clancy, 2005) found H<sub>2</sub>O abundances varying between 0 and 3.5 ppmv with dominant variations to be on short term time scales of 1–2 months. Gurwell et al. (Gurwell et al., 2007) results agreed with those of Sandor and Clancy (Sandor and Clancy, 2005), however he also observed a dramatic factor of 50 decrease in water vapor over a period of 48 h. Sandor and Clancy (Sandor and Clancy, 2005) also noted that there appeared to be more water vapor during the 1998–2001 period than the 2002–2004 period, however, due to the coarse sampling of these observations, neither diurnal or long term variations were positively identified.

The lower mesospheric thermal infrared observations by Encrenaz et al. (Encrenaz et al., 2016; Encrenaz et al., 2013; Encrenaz et al., 2012b) show consistent water vapor abundances between 1 and 1.5 ppmv varying only by a factor of 2, with no spatial variations across the disk.

Previous water vapor observations are summarized in Table 1.

VEx operated in orbit from April 2006 until December 2014, delivering a powerful array of instruments for observing the Venus mesosphere and thermosphere in more detail than previously possible. Observations made by VEx instruments benefited from excellent spatial resolution and also temporal resolution being restricted solely by 24 h orbit. This ability allows temporal variations to be characterized in unprecedented detail. The above cloud water vapor was targeted by SPICAV-IR (Fedorova et al., 2016), VIRTIS (Cottini et al., 2015) and SOIR (Bertaux et al., 2007; Fedorova et al., 2008) instruments. The SPICAV-IR and VIRTIS instruments observed water vapor at or just above the cloud top (~60 km), whilst SOIR is unique in its ability to measure water vapor vertical profiles (80–125 km) through most of the

Venus mesosphere (65 km–130 km). SOIR uses the solar occultation geometry, and as a result observations by SOIR are restricted to morning and evening observations at the Venus terminator (Vandaele et al., 2016a).

Both SPICAV and VIRTIS teams reported small short term variability in the above cloud water vapor, and no diurnal or long term variability, although Cottini et al. (Cottini et al., 2015) reports values for high latitude water vapor abundance were higher for 2009–2011 than they were for the period of 2006–2008. Previous studies by Bertaux et al. (Bertaux et al., 2007) and Fedorova et al. (Fedorova et al., 2008) using a limited sample of SOIR data showed little variability in the profiles, but outlined a depletion in water vapor between 80 and 90 km altitude. There was no abrupt decrease of water vapor with altitude however indicating that condensation at higher altitudes did not occur (Bertaux et al., 2007).

This paper describes the H<sub>2</sub>O profiles obtained from SOIR/VEx observations, as well as the derived abundances and the observed variability throughout the instruments lifetime (2006–2014). We note that SOIR was also sensitive to HDO. However, these data are not described in this paper and will be presented in a future work, as this work is still ongoing. Correlations between water abundance and other species and temperature will also be presented in another paper.

## 2. Instrument

A brief description of the instrument will be supplied here as more detailed descriptions of SOIR can be found in previous publications (Mahieux et al., 2008; Mahieux et al., 2009; Nevejans et al., 2006; Vandaele et al., 2013). SOIR is an IR spectrometer sensitive to the range of 2257–4430 cm<sup>-1</sup> (2.29–4.43 μm). The echelle grating splits the light into 94 diffraction orders numbered 101–194. A TeO<sub>2</sub> Acousto-Optic Tunable Filter (AOTF) placed after the entrance optics allows the selection of diffraction orders, which has a sinc<sup>2</sup>-like transfer function with an in-flight measured Gaussian of 24 cm<sup>-1</sup> full width at half maximum (FWHM), which is larger than the free spectral range of the echelle grating (Mahieux et al., 2008). Therefore, there is an overlap of the diffraction orders adjacent to the targeted order that need to be accounted for. When interpreting the spectra, the contribution of three orders on each side of the selected order is considered.

Up to four different orders can be measured cyclically during a single solar occultation, the same order being measured every second. The observations have a high signal to noise ratio (SNR) ranging from 250 to 3000 (Vandaele et al., 2013). SOIR resolution ranges from 0.11 to 0.21 cm<sup>-1</sup>, spectral sampling from 0.061 to 0.117 cm<sup>-1</sup> and the spectral interval on the detector varies from 19.4 cm<sup>-1</sup> to 37.2 cm<sup>-1</sup>, with increasing order. 32 lines of the detector are illuminated in its spatial direction. Telemetry limits the SOIR instrument to send only eight spectra per second to the Earth, for this reason the detector spatial lines have to be binned on-board into two spatial bins. Before orbit 332, two bins of 16 lines were used, but low signal on the side lines forced us to use after that orbit two bins of 12 lines.

## 3. Observations

In the solar occultation geometry different altitudes of the Venus atmosphere are sounded by tracking the Sun as it sets and rises as viewed from VEx. Therefore SOIR observations always occur at the morning and evening sides of the terminator (6 AM or 6 PM LST). The vertical sampling (the vertical distance between the altitudes of two successive soundings measured at the centre of the projected slit) and the vertical resolution (the vertical altitude range sounded by the projected slit on the atmosphere at that time) are dependent on the orientation of the instrument slit with respect to the planet's surface and on the orbital position of the satellite and therefore the latitude of the tangent point of observation. Due to the orbital positions, the vertical sampling is a maximum of 200 m at 45° North which degrades to 2 km at the North

**Table 2**

List of orders used to target H<sub>2</sub>O. The first column gives the order number, the second and the third the order spectral boundaries, the fourth column the H<sub>2</sub>O observed vibrational transitions in terms of vibrational quantum numbers ( $v_1, v_2, v_3$  in HITRAN notation), and the last column gives the typical sensing height range.

Order	Wavenumber	Wavenumber	Vibrational transition	Sensing height range
Number	Min [cm <sup>-1</sup> ]	Max [cm <sup>-1</sup> ]	( $v_1v_2v_3$ )	[km]
139	3106.4	3133.1	020-000	65-90
144	3218.1	3245.8	020-000	65-80
145	3240.5	3268.3	020-000	65-80
168	3754.5	3786.7	001-000	85-105
169	3776.8	3809.3	001-000	70-110
170	3799.2	3831.8	001-000	80-120
171	3821.5	3854.4	001-000	70-130
172	3821.5	3876.9	001-000	80-120
173	3866.2	3899.4	001-000	80-110
174	3888.6	3922.0	001-000	80-110
175	3910.9	3944.5	001-000	70-100
176	3933.3	3967.1	001-000, 100-000, 020-000	65-85
180	4022.7	4057.2	001-000	65-90
181	4045.0	4079.8	001-000	65-80
182	4067.4	4102.3	001-000, 100-000	65-75
183	4089.7	4124.8	001-000, 100-000	65-75

Pole and 5 km at the South Pole.

Since SOIR has the ability to observe four diffraction orders at each occultation, it allows multiple species to be targeted almost simultaneously. In this study only observations where CO<sub>2</sub> together with water are observed in the same occultation series are used. Hence, measuring CO<sub>2</sub> allows us to derive the pressure and temperature profiles (Mahieux et al., 2015a; Mahieux et al., 2010; Mahieux et al., 2012) and using the CO<sub>2</sub> volume mixing ratio (VMR) from VIRA (Venus International Reference Atmosphere, (Hedin et al., 1983; Zasova et al., 2006)) the volume mixing ratio of water vapor can be calculated. The altitude range probed depends on the strength of the targeted molecular absorption features; in general SOIR observations are sensitive to CO<sub>2</sub> from 65 km to 160 km and H<sub>2</sub>O from 80 km to 125 km. This study measures H<sub>2</sub>O across several orders (see Table 2).

Fig. 1 shows the locations and strengths of H<sub>2</sub>O, CO<sub>2</sub> and HF absorption ro-vibrational lines in the orders used for H<sub>2</sub>O detection. The position and line intensities are from HITRAN 2012 (Rothman et al., 2013) corrected for the Venus atmosphere, i.e. pressure broadening coefficients are modified to take into consideration that CO<sub>2</sub>, rather than N<sub>2</sub> and O<sub>2</sub> as on Earth, is the dominant atmospheric gas on Venus (Gamache et al., 2016).

HITRAN intensities have been multiplied by typical values of volume mixing ratio for the Venus atmosphere: 96.5% for CO<sub>2</sub>, 2 ppm H<sub>2</sub>O and 300 ppb for HF. These figures were obtained for temperature and pressure conditions characteristic of an altitude of 80 km on Venus: 215

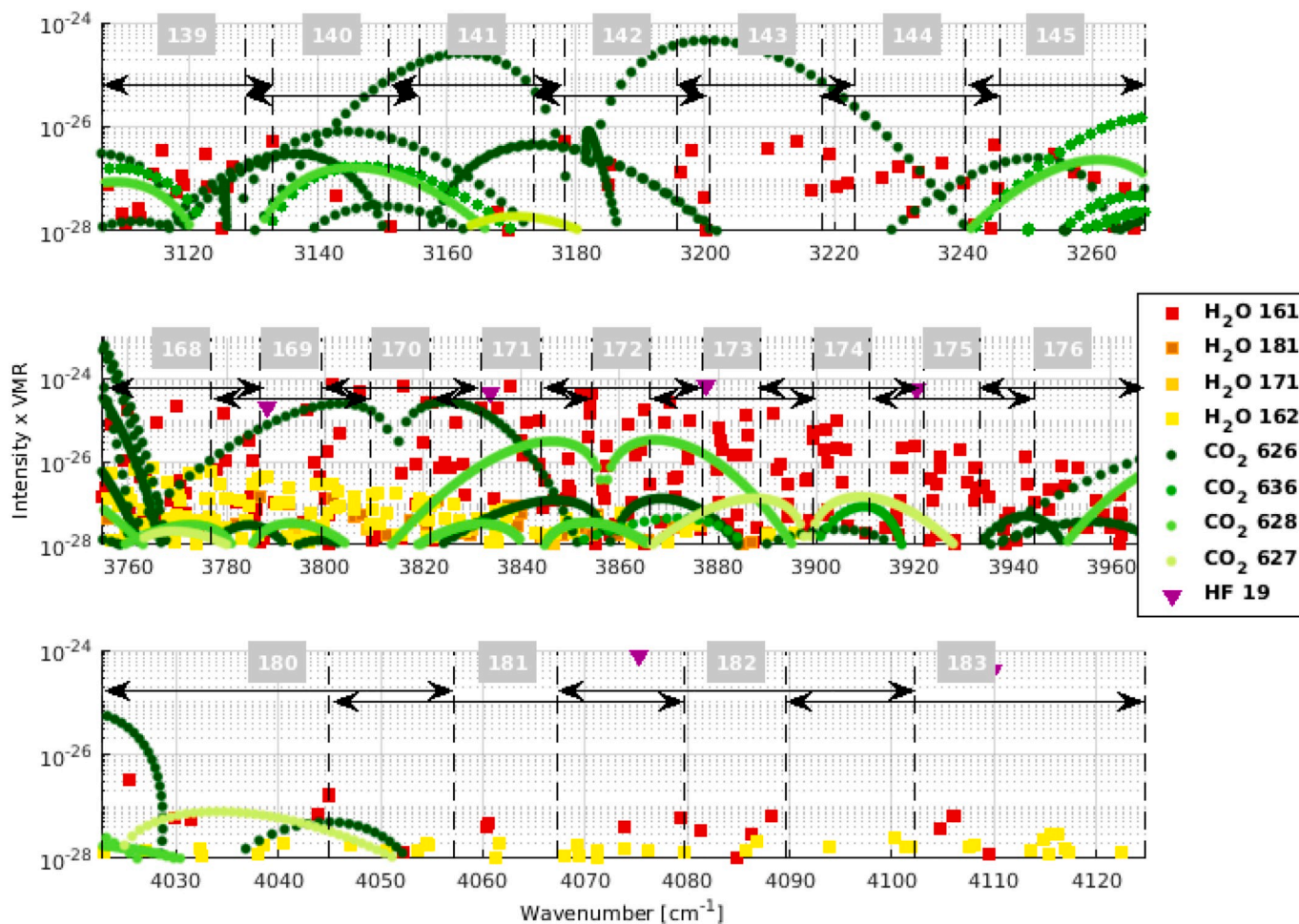


**Fig. 1.** Intensity of the H<sub>2</sub>O (squares), CO<sub>2</sub> (dots) and HF (triangles) lines as given in HITRAN 2012 (Rothman et al., 2013) for typical temperature and pressure (215 K and 3.27 mbar) found on Venus at 80 km of altitude as a function of the wavenumber, multiplied by typical Venus VMR (96.5% for CO<sub>2</sub>, 2 ppm for H<sub>2</sub>O and 300 ppb for HF). Each isotopologue is given in a different color (see legend). The order boundaries are given by the vertical black dashed lines, and the order numbers are printed on the top of each panel, and their extents by the horizontal arrows. Note: in the top panel only orders 139, 144 and 145 were used for H<sub>2</sub>O studies.

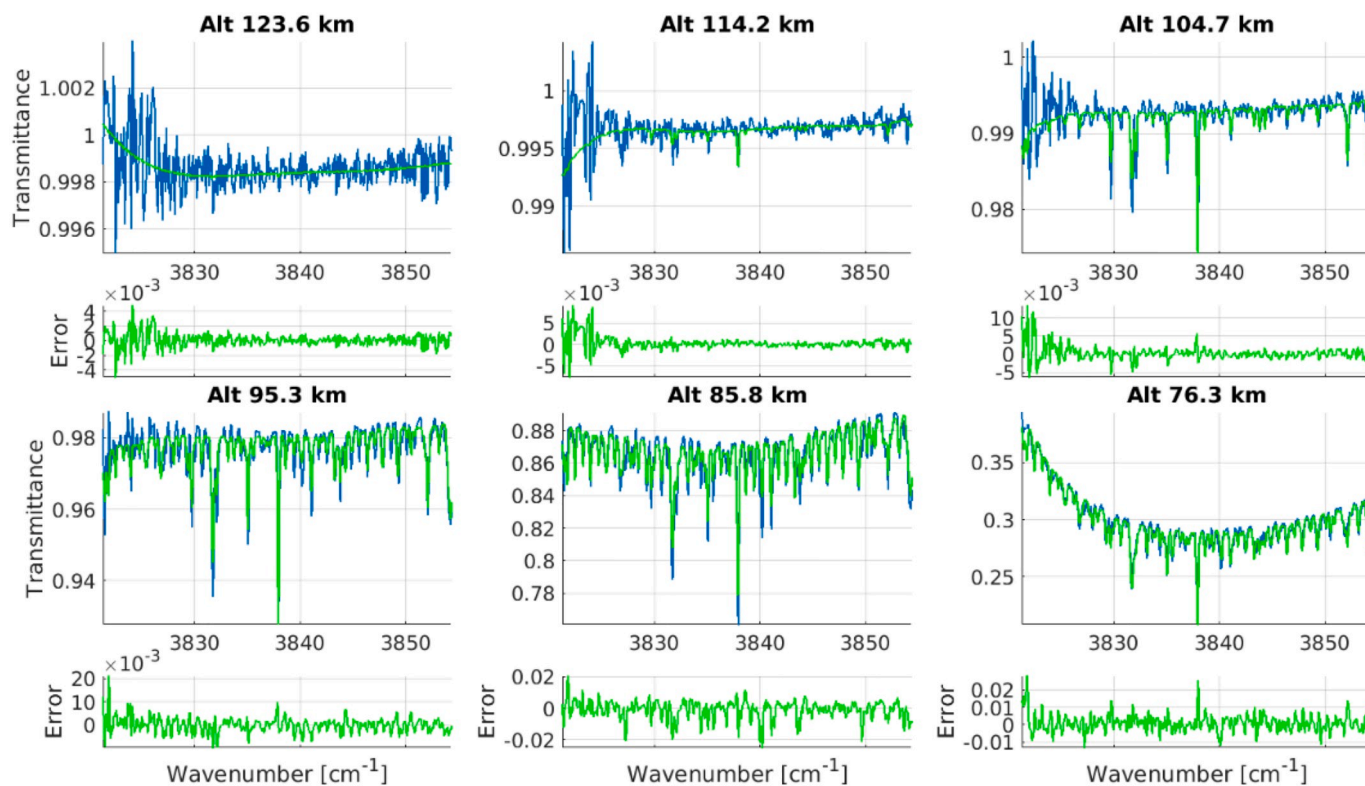


Fig. 2. Example of spectral fit from orbit 1029.1, order 171, bin 1, for six spectra in the altitude range 76 to 123 km. That particular solar occultation occurred at  $65^\circ$  latitude South,  $125^\circ$  longitude, 6 AM on 130/02/2009. In the upper figure of each panel, the blue spectrum is the SOIR transmittance spectrum (Trompet et al., 2016), the green spectrum is the synthetic spectrum. The residuals are plotted in the bottom part of each panel. (For interpretation of the references to color in this figure legend, the reader is referred to the web version of this article.)

K and 3.27 mbar.

H<sub>2</sub>O has three main strong vibrational transitions ( $\nu_1\nu_2\nu_3$  for the upper and lower vibrational state respectively, in HITRAN notation) 001–000, 100–000 and 020–000 across the SOIR spectral range that appear from orders 125 to 194 ( $2794$  to  $4373$   $\text{cm}^{-1}$ ). Their spectral lines are partially hidden by much stronger CO<sub>2</sub> absorption bands. The orders chosen are the spectral regions where H<sub>2</sub>O lines are clearly distinguishable from CO<sub>2</sub> absorption lines.

#### 4. Measurement technique and simulation of spectra

The solar occultation technique is used to study the vertical structure and composition of the Venus atmosphere. Solar reference radiance spectra are sampled far off the planetary limb prior or post every observation scan. SOIR then sounds the atmosphere of the planet at different tangent altitudes at sunset or sunrise where it records solar atmospheric radiance spectra, where the atmospheric lines have absorption lines. The transmittance spectra are obtained by dividing the solar atmospheric radiances by the solar radiances (Trompet et al., 2016). The orientation of the SOIR slit should be tangential to the planetary limb, however rotations of the slit were caused as VEx moved along its orbit in inertial mode, and slightly enlarged the vertical resolution. The attitude of VEx was calculated using the Spice routines developed by NAIF (NASA Ancillary Information Facility, (Acton, 1996)).

The synthetic transmittance due to all molecular species present along the line of sight, which corresponds to the projected centre of the slit on the limb at each single measurement, is obtained by multiplying the absorbance of all molecules in all the sampled layers. A layer is an atmospheric segment between two altitudes defined by the centre of the slit at the impact point of two successive measurements, over which temperature and pressure are interpolated. The molecular absorption

cross sections in each layer are dependent on temperature, pressure and partial pressure and are calculated by a line by line procedure described in Vandaele et al. (2008). The decrease of the spectral baseline is linked to the solar light extinction by aerosols present along the line of sight (Wilquet et al., 2012; Wilquet et al., 2009). Over the spectral range of a diffraction order, their signature is a continuum of absorption without any fine structures therefore a polynomial of maximum order 5, typically 2, is usually good enough to reproduce this baseline. The final synthetic transmittance spectrum is a unity transmittance spectrum attenuated by the effect of the atmospheric molecular species and aerosols, and then convolved by the instrumental function. The instrumental function takes into account the previously mentioned difference between the free spectral range of the echelle grating and the bandwidth of the AOTF, the physical size of the slit and its effect on vertical resolution. Improvements in algorithm retrieval described in Mahieux et al. (2015a), take into consideration 24 light paths spread across the slit in both spatial and spectral directions and used to calculate the average contribution of all paths to determine altitude and latitude. Such a spectral inversion procedure accounts for the variable vertical sampling and vertical resolution, such that the vertical profiles are in the end independent of such effects.

#### 5. Retrieval procedure

The retrieval method to obtain number density and temperature profiles was described in Mahieux et al. (Mahieux et al., 2010; Mahieux et al., 2012) and was already successfully applied on SOIR spectra for the analysis of other trace gases in the Venus atmosphere such as CO (Vandaele et al., 2016b; Vandaele et al., 2015), SO<sub>2</sub>, (Mahieux et al., 2015b; Vandaele et al., 2017a; Vandaele et al., 2017b), HCl or HF (Mahieux et al., 2015d). A short summary is provided here.

The ASIMAT algorithm is an iterative procedure consisting of two

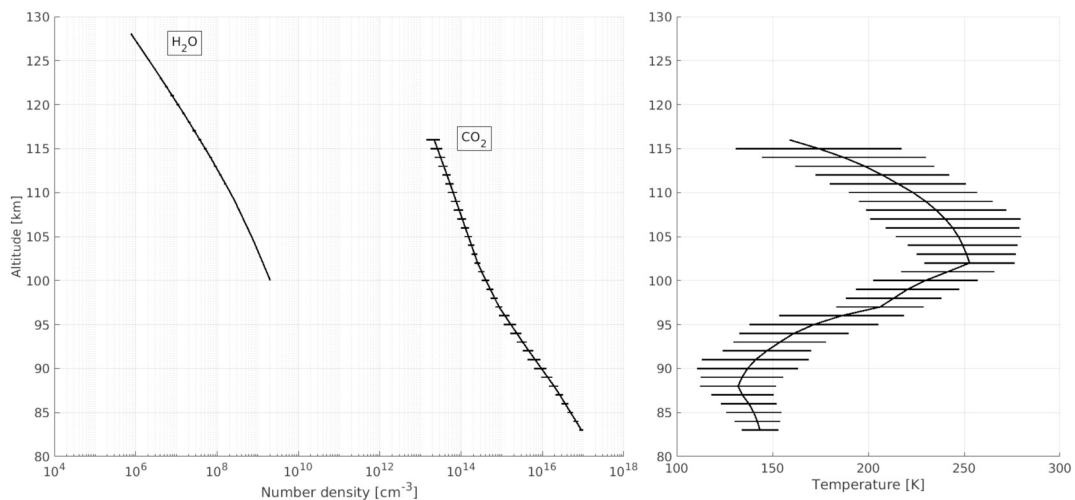


**Fig. 3.** Orbit 1029.1, 65° latitude South, 125° longitude, 6 PM, measured on 13/02/2009. Left panel: Retrieved CO<sub>2</sub> and H<sub>2</sub>O number density profiles derived from transmittances measured in order 171 bin 1. The horizontal bars are the uncertainties. Right panel: Retrieved temperature vertical profile with error bars in the same altitude region.

main steps. In the first step, non-saturated atmospheric transmittance spectra are fitted using the Rodgers Bayesian method (Rodgers, 2000) in a plane parallel atmosphere, if their corresponding synthetic atmospheric transmittance at the SOIR spectral resolution is larger than 0.15 (Mahieux et al., 2012), to avoid line saturation issues. The independent number density profiles of the species that absorb in each of the

observed orders for that occultation are calculated over discrete layers, over which parameters are considered to vary hydrostatically. During this step, the synthetic spectra are fitted to the measured spectra, and the logarithm of the number density profiles is adjusted for given temperature and pressure profiles. In the second step, the independent number density profiles from the different orders and bins are combined using a

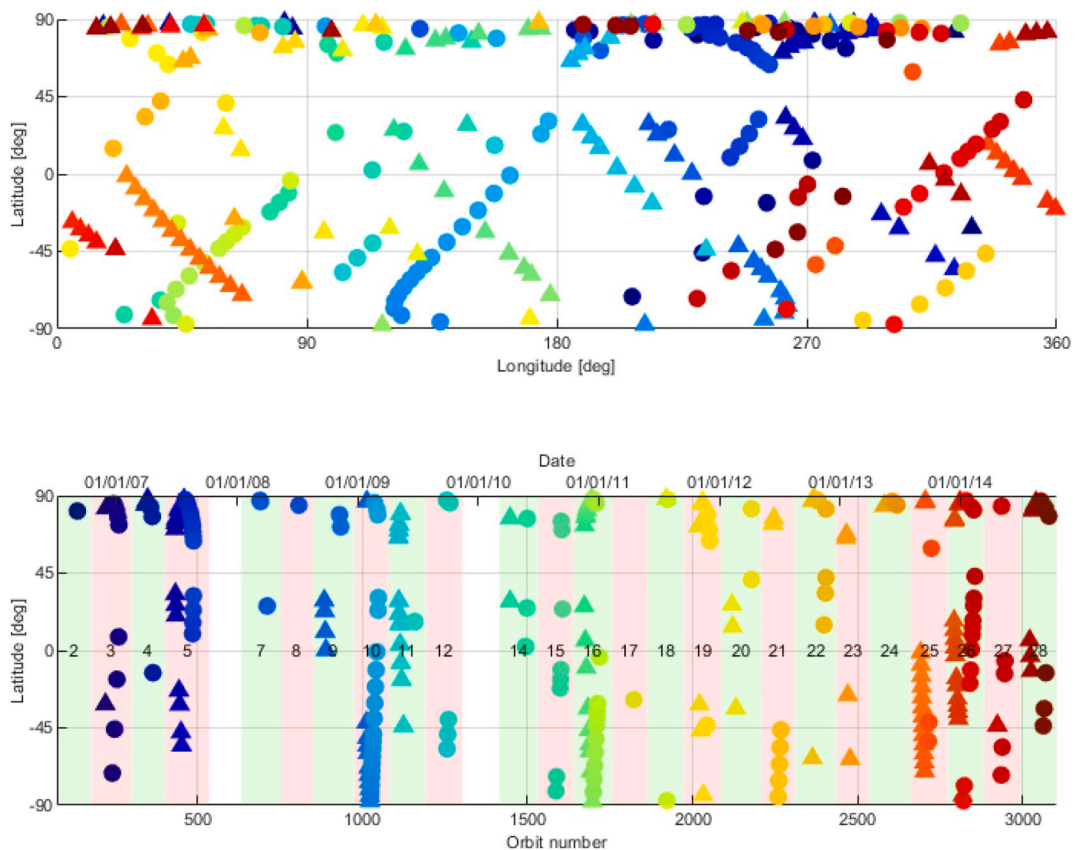


**Fig. 4.** Observations of H<sub>2</sub>O considered in this study made by SOIR during the entire VEx mission. The upper panel shows latitude by longitude and the lower panel shows latitude by time (orbit numbers span >8 Earth years from April 2006 till November 2014). First day of the year are indicated for information. The numbers in the center of the panel are the occultation seasons. All observations are made either at the morning (circle) or evening (triangle) side of the terminator. The colors is the time along the mission, from blue (06/2006) to red (12/2014). (For interpretation of the references to color in this figure legend, the reader is referred to the web version of this article.)

weighted linear moving average procedure (Mahieux et al., 2012; Vandaele et al., 2015), which we name best-fit profiles. The temperature profile is calculated from the CO<sub>2</sub> number density profile derived from SOIR spectra using the hydrostatic law and assuming the CO<sub>2</sub> VMR from VIRA (Hedin et al., 1983; Zasova et al., 2006). Finally, the pressure is updated. The a-priori number density and temperature profiles for the new step are taken as the best-fit profiles from the previous step. The inversion is considered to have converged when the number density of all retrieved species and the temperature profiles are within the uncertainty of the previous step. CO<sub>2</sub> VMR is not updated since it is always considered to be equal to the one from VIRA (Hedin et al., 1983; Zasova et al., 2006).

During the Bayesian inversion, we consider covariance values equal to 25% for the logarithm of the number densities and the noise in the spectra in order to minimize the dependence of the retrieved species density on the a priori density. At the first step, the a priori values for H<sub>2</sub>O are taken considering a constant 1 ppm volume mixing ratio profile.

The six spectra shown in Fig. 2 are examples of typical H<sub>2</sub>O spectral fits. Altitudes between 76 and 123 km are shown from orbit 1029.1 (the decimal is used to decipher between observations taken during the same orbit), order 171, bin 1. The absorption line shape is approximated using a Voigt profile and the fit is seen to degrade below 95 km at some wavenumbers. This is explained by absorptions at those wavenumbers becoming saturated at lower altitudes resulting in a poor fit with the Voigt approximation. We also note that the SOIR resolution does not resolve the assumed Voigt profile line shape.

The resulting H<sub>2</sub>O number density profile, the simultaneously measured CO<sub>2</sub> number density profile and the derived temperature profiles, are given in Fig. 3 together with their uncertainties.

## 6. Calibrations and uncertainties

The noise on the spectra is obtained directly from the measurement itself, by calculating the signal to noise ratio, as described in Vandaele et al. (2013) and Trompet et al. (2016). The uncertainty on the vertical density profiles of CO<sub>2</sub> and H<sub>2</sub>O are directly obtained from the Bayesian algorithm, and the method is discussed in Mahieux et al. (2012) and Mahieux et al. (2015a). The uncertainty on the temperature profile is obtained from the hydrostatic equilibrium, accounting for the error on the CO<sub>2</sub> density profile, using a statistical approach, as described in Mahieux et al. (2015a). The uncertainty on the VMR is obtained from the uncertainties on the CO<sub>2</sub> and H<sub>2</sub>O number density profiles.

The uncertainty on the retrieved temperature profile is not negligible (from 5 to 50 K): we note that there is a strong temperature dependence on the gases absorption cross sections in the infrared (Mahieux et al., 2015a). For that reason, we should address the retrieved abundance dependence on the temperature profile. Such a study has been done in Vandaele et al. (2015) for CO, where a series of temperature profiles is used to perform a spectral inversion using ASIMAT. The conclusion of this study is that the variations in the retrieved number density profiles remains small compared to the uncertainty on the number density profile. The root-mean-square (RMS) of the fit should always be controlled on the converged solution, which has always been the case in this study. Hence, because the temperature profile influences the relative deepness of the absorption features, an offsetted temperature profile is directly seen in the spectral fit, and is used as a criterion to reject a profile. This criterion has been used for 23 orbits, which are thus not considered in the database presented here.

The SOIR spectral features are not dependent on the pressure profile. Hence, the pressure induces a spectral enlargement of the absorption lines, but which remains always smaller by at least one order of magnitude with respect to the SOIR spectral resolution. Recently, new H<sub>2</sub>O line parameters were measured in a CO<sub>2</sub> buffer gas cell (Régalia et al., 2019). The impact of the pressure broadening with these new parameters still needs to be quantified, but will probably not affect the SOIR retrievals because of the much broader spectral resolution of the

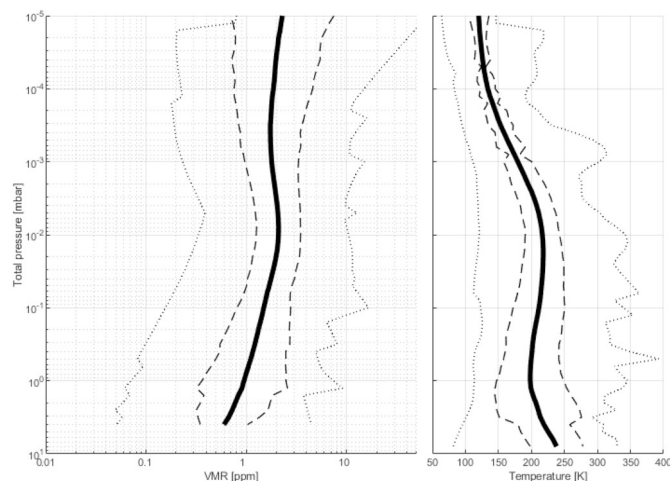


**Fig. 5.** Water vapor volume mixing ratio (left panel) and temperature (right panel) as a function of the pressure, averaged (solid lines) from data considered in this analysis, obtained at all latitudes and at both local solar times. The dashed lines show the standard deviation of data at each pressure level. The dotted lines are the maximum and minimum value ranges.

instrument compared to the width of the water atmospheric lines.

## 7. Results

This study includes 287 of 369 observations of water vapor (Fig. 4) for which CO<sub>2</sub> observations were obtained simultaneously to access information on the volume mixing ratio. Observations were omitted when the applied retrieval procedure described in Section 5 failed to converge or the criteria mentioned in Section 6 were not met.

### 7.1. Average profile

The H<sub>2</sub>O VMR profile is obtained by multiplying the ratio between the H<sub>2</sub>O density profile and the CO<sub>2</sub> density profile, by the VIRA CO<sub>2</sub> VMR profile.

Fig. 5 (left panel) shows the average water vapor abundance vertical profile across the full 8 years of observations (solid line), standard deviation (dashed lines) and minimum and maximum value ranges (dotted lines). The average profile is calculated as a function on the pressure scale rather than the altitude scale to remove the global atmosphere variability, when at least five individual profiles exist for a pressure level (Mahieux et al., 2015d). The average profile can be seen as uniform, considering the large dispersion observed in the measured profiles. The mean profile shows a characteristic weak local maximum of 2 ppmv at  $\sim 0.01$  mbar/ $\sim 103$  km and a much less manifest local minimum of 1.8 ppmv at  $\sim 0.003$  mbar/ $\sim 115$  km. The minimum abundance (0.56 ppmv) is located at the highest pressures/lowest altitudes (3 mbar/ $\sim 80$  km) and the highest abundance (2.4 ppmv) is located at the lowest pressures/highest altitudes ( $10^{-5}$  mbar/ $\sim 125$  km). The standard deviation is significantly smaller than the variability from orbit to orbit indicating that it is not a product of uncertainties and although the range of volume mixing ratio values at 0.01 mbar/ $\sim 100$  km (0.1 ppmv to 9.1 ppmv) span almost 2 orders of magnitude, these are consistent with previous results from thermal infrared (Encrenaz et al., 2016; Encrenaz et al., 1995; Encrenaz et al., 1991; Sandor and Clancy, 2005) and sub-mm observations (Gurwell et al., 2007), as summarized in Table 1.

The thermal structure and relevant variations, uncertainties and errors in temperature have been thoroughly addressed in Mahieux et al. (2012), Mahieux et al. (2015a) and Mahieux et al. (2015c). However, it is worth noting that the local maximum in water vapor VMR occurs at all latitudes between the pressures/altitudes of  $\sim 0.02$  mbar/ $\sim 95$  km and 0.01 mbar/ $\sim 105$  km and corresponds to a local temperature maxima

**Table 3**

Latitude bins statistics of the mean profiles presented in Fig. 6.

Latitude bin	North	South
0°–20°	21	22
20°–60°	24	58
60°–90°	128	34

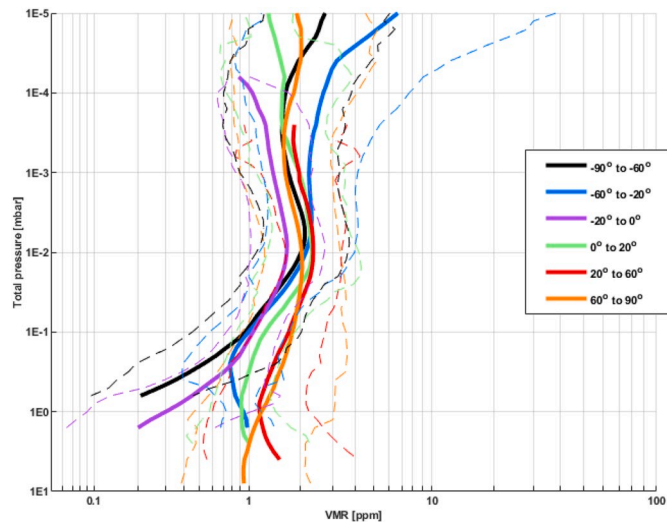


Fig. 6. The profiles are given on a log scale, and are averaged on the pressure scale for different latitude bins. The error weighted standard deviations are given by the dashed curves.

near 100 km (see Fig. 5, right panel).

## 7.2. Spatial variability

### 7.2.1. Latitudinal variability

Venus is often assumed to be symmetric about the equator, however in this study north and south latitude bins were not combined as the asymmetric orbital path of the Venus Express spacecraft meant that the northern hemisphere observations were more frequent (Table 3) and had a higher vertical spatial resolution than those of the southern hemisphere, as described in Section 3. Spectral bins were therefore kept separated to determine if spatial resolution imposed significant profile errors between the hemispheres. The Venus Express orbit also meant that no observations were obtained between 45 and 60° North (Fig. 4) and so latitude bins were carefully chosen to ensure that a statistically significant number of observations were included in each bin. The six latitude bins chosen are symmetric about the equator to allow for hemispheric comparisons: 60–90° (polar bins), 20–60° (mid-latitude bins) and 0–20° (equatorial bins), see Table 3 for statistics.

The average VMR profiles (solid lines) for each latitude bin (Fig. 6) behave similarly to the VMR profile averaged over the whole dataset (Fig. 5). In Fig. 6, the abundance differences between each latitudinally averaged profile (solid lines), between the pressures/altitudes of ~0.02 mbar/~90 km and 0.003 mbar/~117 km, are within the standard deviation of each averaged profile (dashed curves). Therefore we can conclude that no significant latitudinal variations are observed in this data set and a hemispherical symmetry can be assumed for averaged profiles.

### 7.2.2. Local solar time (LST) variability

Continuing from the previous analysis, we now assume a hemispheric symmetry and bin H<sub>2</sub>O VMR profiles by absolute latitude and LST (morning or evening observations) using the whole dataset. The profile split statistics are provided in Table 4.

**Table 4**

Number of orbits statistics of the mean profiles presented in Fig. 6.

Latitude bin	Morning side	Evening side
0°–20°	22	21
20°–60°	40	42
60°–90°	90	72

Each profile in Fig. 7 shows similar trends to the globally averaged profile shown in Fig. 5. Each bin averaged profile shows a local maximum near 0.01 mbar/~100 km at both the morning and evening sides of the terminator, albeit the polar evening profile (Fig. 7c – red solid line) shows an extended and slightly lower altitude maximum. The equatorial averaged profiles also show a steeper abundance gradient below 0.01 mbar/~100 km than the polar profiles for both the morning and evening terminator. Finally, we note that at each latitude bin, the differences between the morning and evening terminator VMR averaged profiles (solid lines) are within the standard deviation margins (shaded regions) of both the morning and evening observations and therefore we do not see any significant differences between morning and evening vertical H<sub>2</sub>O abundance profiles for any latitude bin.

## 7.3. Temporal variability

### 7.3.1. Long term temporal variability

In Fig. 8, panels A to D show the H<sub>2</sub>O VMR of individual observations versus orbit number for various pressure levels/altitudes. An increase in water vapor VMR is seen in the first 500 orbits for pressures below 10<sup>-2</sup> mbar/~102 km (panel C and D) and is observed for all latitudes. This increase is seen in other molecular species, as well as for the aerosol content in the upper haze, observed by SOIR and other Venus Express Instruments (Cottini et al., 2015; Mahieux et al., 2015d; Marcq et al., 2011; Marcq et al., 2013; Vandaele et al., 2016b; Wilquet et al., 2012).

It is tempting to identify long-term structure in the data, however investigation indicates that the suggested variations do not neatly correspond to local solar time nor seasonal frequencies. These apparent long-term trends vary by less than an order of magnitude and the non-regular sampling rate and larger short-term variability (see next paragraph) of typically an order of magnitude, rule out any meaningful analysis. Therefore, no long-term cycles are clear from this dataset.

### 7.3.2. Short term variations

Short term variations dominate the dataset commonly varying by one order of magnitude over a 24 h period. The largest water vapor VMR difference we observe in our dataset within a period of 24 h is a factor of 20, compared to the factor of 50 observed by Gurwell et al. (2007). Figs. 9 and 10 look closely at two periods of about 50 Earth days where observations of water vapor were taken at regular time intervals. While the observations cover a broad range of latitudes in Fig. 9, they are restrained to high Northern latitudes in Fig. 10 as illustrated in color bars. The figures present VMR values for water at constant pressure level, coloured by latitude – red (poles) to blue (equator) and shaped by LST (circle – 6 AM and triangle – 6 PM). Each figure typically shows a H<sub>2</sub>O VMR variation range of about one order of magnitude across both time periods.

In the example shown in Fig. 9, the general shape of the H<sub>2</sub>O VMR variations is similar at the two highest pressure levels; there is an overall decrease of H<sub>2</sub>O abundance from orbit 1012 (27/01/2009, latitude 41°S) to 1025 (09/02/2009, latitude 82°S), then show a sudden increase of water vapor. H<sub>2</sub>O abundance steadies by orbit 1032 (16/02/2009, latitude 52°S), at a higher abundance than previously, and gradually decreases again to orbit 1048 (04/03/2009, latitude 35°N). This pattern is less clear at the highest altitude although not completely absent. Due to the orbital progression covering 120° of latitude, there is a possibility that these variations may be partly due to the changing latitude and the data would therefore indicate that there is a decrease in H<sub>2</sub>O of

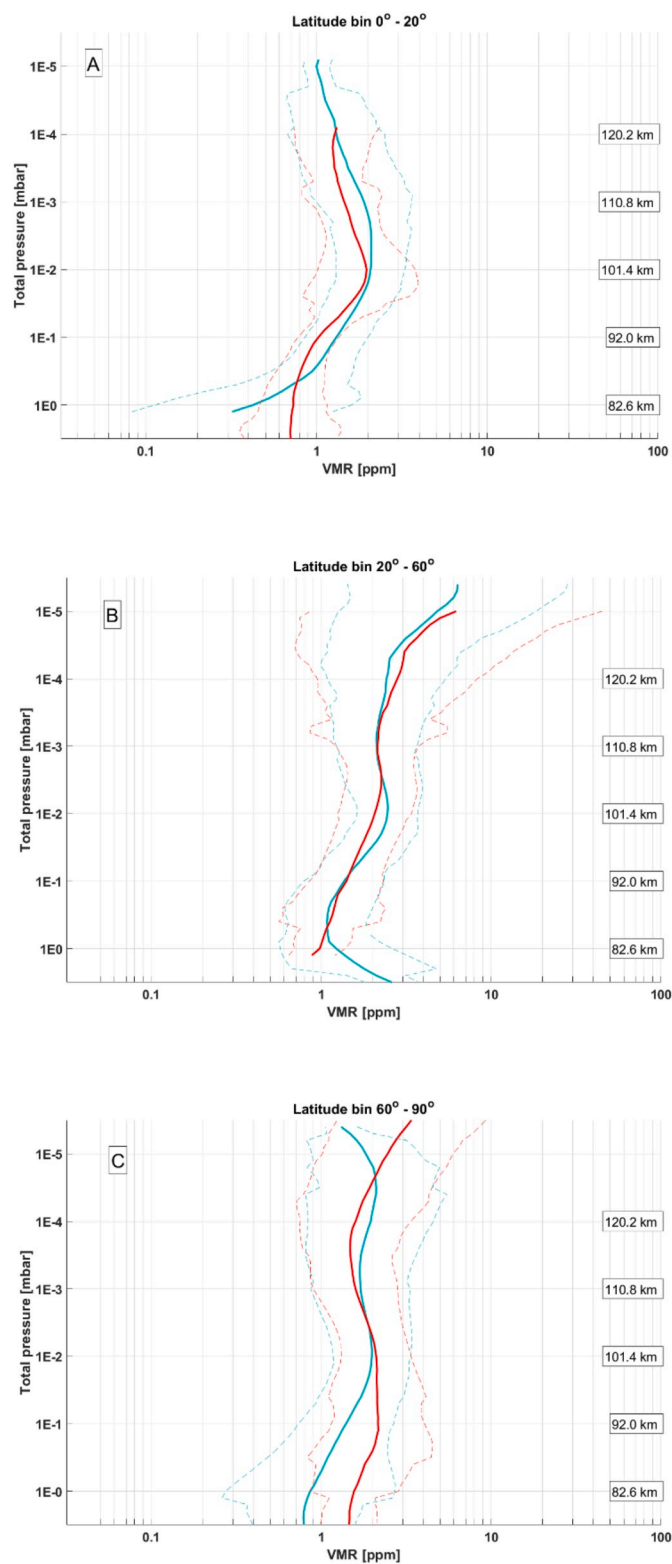
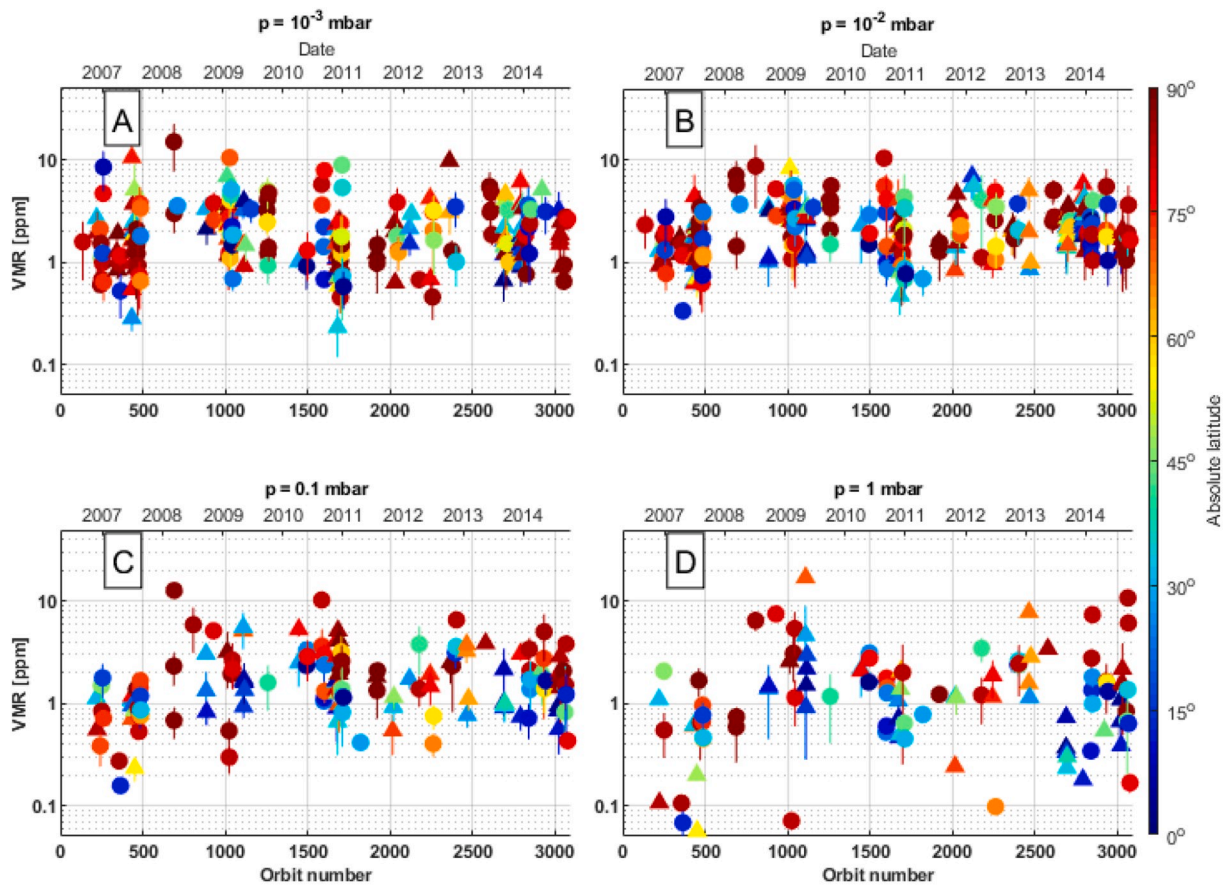
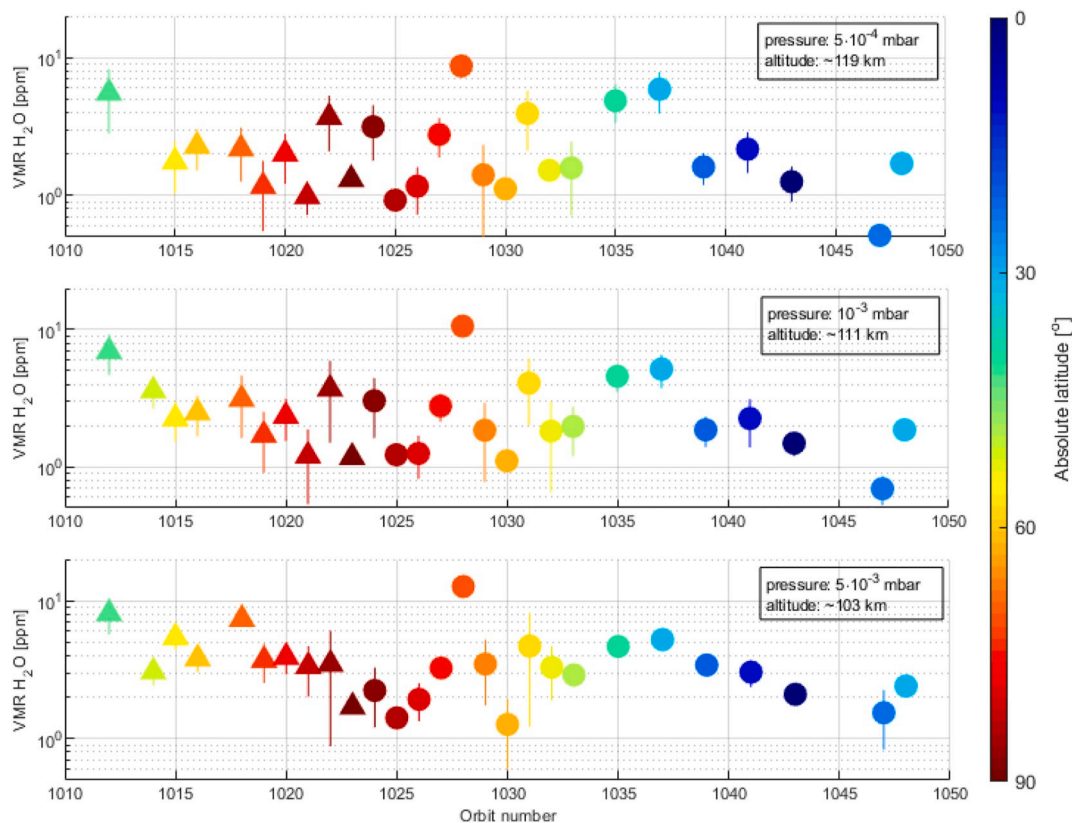


Fig. 7. Average profiles for morning (blue) and evening (red) sides of the terminator for latitude bin  $0^\circ - 20^\circ$  (equatorial latitudes, Panel A),  $20^\circ - 60^\circ$  (mid-latitudes, Panel B) and  $60^\circ - 90^\circ$  (polar latitudes, Panel C). Equatorial symmetry is assumed. The dashed lines are the error weighted standard deviations. (For interpretation of the references to color in this figure legend, the reader is referred to the web version of this article.)



**Fig. 8.** H<sub>2</sub>O VMR in ppm with time (~8 Earth years) for four pressure levels: 10<sup>-3</sup> mbar/~110 km (upper left panel), 10<sup>-2</sup> mbar/~102 km (upper right), 0.1 mbar/~93 km (lower left) and 1 mbar/~84 km (lower right). The first day of the years are indicated at the top of the top panels. Colors depict the absolute latitude, see colorbar, and shapes indicate LST (6 AM: circles and 6 PM: triangles). The vertical bars give the uncertainties.



**Fig. 9.** VMR of water vapor at various pressure/altitude levels for successive occultations:  $5 \cdot 10^{-4}$  mbar/ $\sim 119$  km (upper panel),  $10^{-3}$  mbar/ $\sim 111$  km (middle panel) and  $5 \cdot 10^{-3}$  mbar/ $\sim 103$  km (lower panel). The vertical lines are the VMR error bars. The color code is the absolute latitude from polar (dark red) to equatorial (dark blue) regions, see color bar. All measurements are in Southern hemisphere besides the ones after orbit 1045. Circles (6 AM) and triangles (6 PM) denote the local solar time. The time period spans from January to March 2009. (For interpretation of the references to color in this figure legend, the reader is referred to the web version of this article.)

approximately a factor of 2 over the polar region and equator with respect to the mid-latitudes at the time of observation meaning therefore that the water vapor in the Venus mesosphere is the highest at mid-latitudes.

Fig. 10 presents the same analysis for another period of successive observations confined to a narrower range of latitudes (bin of  $<30^\circ$ ). The pattern of the VMR is very similar for the three pressure levels and the highest change of a factor 15 (at  $5 \cdot 10^{-3}$  mbar) and 18 (at  $10^{-3}$  mbar) in the water vapor abundance is observed between orbit 434 (29/6/2007, latitude  $74^\circ\text{N}$ ) and 435 (30/6/2007, latitude  $76^\circ\text{N}$ ). In this case, the short-term variability cannot be due to a difference in latitude.

Sandor and Clancy (2005) tentatively indicates that across the altitude range of 65–100 km short term variations are most rapid at lower altitudes which precede a change in the upper mesosphere. Our data across a higher overlapping altitude range of 80–120 km does not show a temporal lag in VMR abundance changes between different altitude ranges. Figs. 8–10 rather indicate that changes in water vapor abundance can happen simultaneously across large pressure/altitude levels in bulk, rather than a gradually settling of water vapor abundance or injections at different levels.

#### 7.4. Atmospheric structure and dynamics

The sub 100 km region is identified as a dynamically chaotic altitude region where the Sub Solar to Anti Solar (SSAS) wind regime above 100 km transitions to the strong global circulation regime observed in the clouds  $\sim 70$  km (Bougher et al., 1988). In this region the average  $\text{H}_2\text{O}$  VMR profile increases with altitude from 80 km and reaches a local maximum at approximately 100 km. The average temperature is also seen to increase through this same altitude range and includes some of

the largest observed temperature ranges, peaking at maximum temperatures around 100 km (Sandor and Clancy, 2005). The decrease in  $\text{H}_2\text{O}$  at 80–90 km with respect to 100 km was previously seen in SOIR data by Bertaux et al. (2007) and Fedorova et al. (2008). Modelling across this altitude region indicates that the temperature structure is due to radiative transfer rather than dynamical processes (Bougher et al., 2015; Mahieux et al., 2020).

## 8. Conclusion

287 water vapor vertical profiles obtained at the Venus terminator between 80 km and 125 km from 13th August 2006 to 25th September 2014 were analysed for temporal and spatial abundance variations. The average atmospheric profile is found to vary with altitude between 0.56 ppmv and 2.45 ppmv which is in good agreement with previous observations (Bertaux et al., 2007; Cottini et al., 2015; Fedorova et al., 2008). Standard deviations are significantly smaller than the full range of volume mixing ratio values at all altitudes indicating that the variations are real, as displayed in Fig. 5.

The decrease in volume mixing ratio abundance below 100 km appears to be a common feature of most water vapor volume mixing ratio profiles and agrees with the decrease in water vapor observed by both Bertaux et al. (2007) and Fedorova et al. (2008). It is difficult to conclude whether the altitude trend of the water vapor VMR is in agreement with the study by Sandor and Clancy (2005) as the altitude range covered by mm-wave ground-based spectra only partly overlaps with the one covered by the SOIR experiment for which the altitude sounded is also much better resolved. Based on a very limited number of spectra, the variability of the water vapor VMR was found to be higher in the lower than in the upper mesosphere of Venus (Sandor and Clancy,

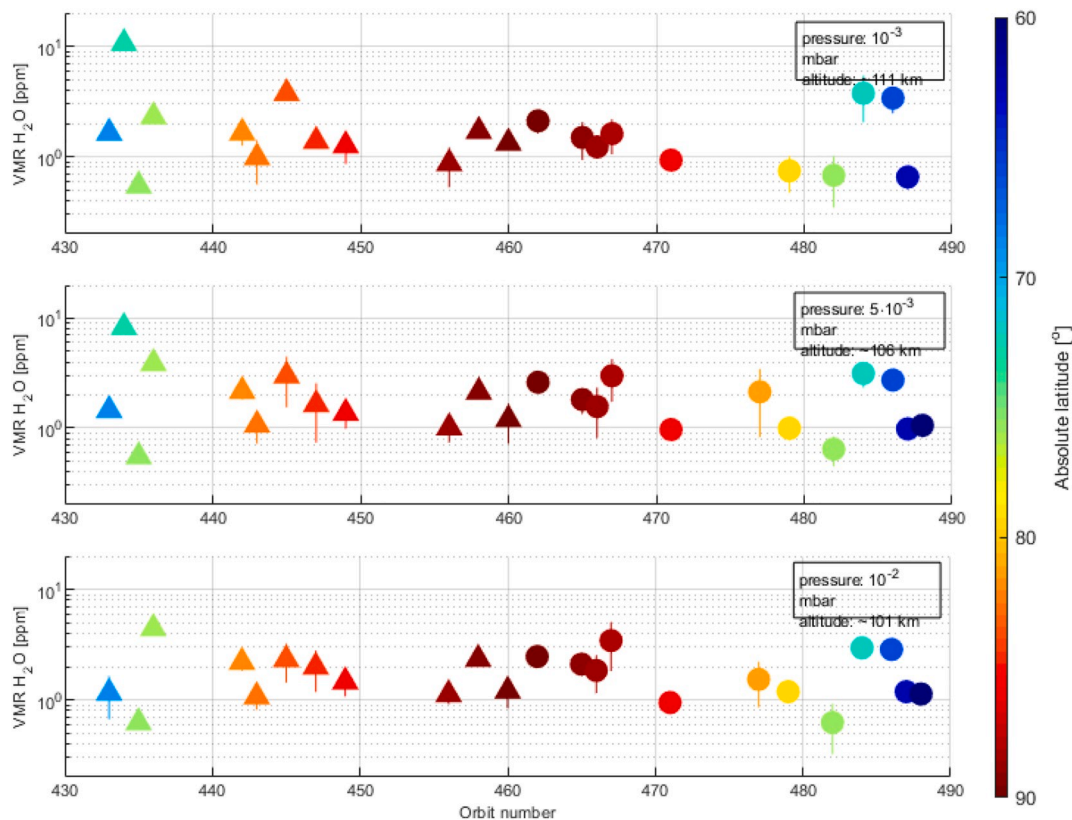


**Fig. 10.** VMR of water vapor at various pressure/altitude levels for successive occultations:  $10^{-3}$  mbar/ $\sim 111$  km (upper panel),  $5 \cdot 10^{-3}$  mbar/ $\sim 106$  km (middle panel) and  $10^{-2}$  mbar/ $\sim 101$  km (lower panel). The vertical lines are the VMR error bars. The color code is the absolute latitude from North Pole (dark red) to  $65^{\circ}$ N (dark blue) and circles (6 AM) and triangles (6 PM) denote the local solar time, see color bar. All measurements are in Northern hemisphere. The time period spans from June to August 2007. (For interpretation of the references to color in this figure legend, the reader is referred to the web version of this article.)

2005); this is in agreement with our observations as the standard deviation of the SOIR mean profile is the smallest at 100 km and increases with decreasing altitude.

No simple trend or cyclic spatial variations or long term temporal variations are observed in the present data set in which short term variability masks all other possible trends. Our observations agree that short term (between 1 and 10 Earth days) variability is dominant. Temporal variability of water vapor commonly varies by up to an order of magnitude in any 24 h period. The largest variation we have observed in 8 years was an increase by a factor of 18 in a 24 h period which occurred at approximately 111 km.

All the water profiles used for the analysis presented in the current study are available on the Virtual European Solar and Planetary Access (VESPA, <http://www.europlanet-vespa.eu/>), which aims at building a Virtual Observatory for Planetary Science, connecting all sorts of data in the field, and providing modern tools to retrieve, cross-correlate, and display data and results of scientific analyses (Trompet et al., 2017). The full Venus Express SOIR dataset is available in the open access VESPA infrastructure (Erard et al., 2017) under the label ‘Venus atmospheric profiles - From SPICAV-SOIR/VEx’. Future datasets relative to HDO measurements will also be added to this repository when the paper dealing with that specie will be published.

## Acknowledgements

Venus Express is a planetary mission from the European Space Agency (ESA). We wish to thank all ESA members who participated in the mission, in particular, H. Svedhem and D. Titov. We thank our collaborators at IASB-BIRA (Belgium), Latmos (France), and IKI (Russia). The research program was supported by the Belgian Federal Science Policy Office and the European Space Agency (ESA, PRODEX program,

contracts C 90268, 90113, 17645, 90323 and 4000107727). We acknowledge the support of Belgian Fonds de la Recherche Scientifique (FNRS) under grant number 30442502 (ET-HOME) and a BRAIN research grant BR/143/A2/SCOOP. The research leading to these results has received funding from the European Union Seventh Framework Programme (FP7/2007-2013) under grant agreement no 606798 (EuroVenus Project). A. Mahieux thanks the F.N.R.S. for the position of ‘chargé de recherche’.

## References

- Acton, C.H., 1996. Ancillary data services of NASA’s navigational and ancillary information facility. *Planet. Space Sci.* 44, 65–70.
- Bertaux, J.L., et al., 2007. A warm layer in Venus’ cryosphere and high altitude measurements of HF, HCl, H<sub>2</sub>O and HDO. *Nature* 450, 646–649.
- Bougher, S.W., Dickinson, R.E., Ridley, E.C., Roble, R.G., 1988. Venus mesosphere and thermosphere. III. Three-dimensional general circulation with coupled dynamics and composition. *Icarus* 73, 545–573.
- Bougher, S.W., et al., 2015. Upper atmosphere temperature structure at the Venusian terminators: a comparison of SOIR and VTGCM results. *Planet. Space Sci.* 113–114, 336–346.
- Cottini, V., Ignatiev, N.I., Piccioni, G., Drossart, P., 2015. Water vapor near Venus cloud tops from VIRTIS-H/Venus Express observations 2006–2011. *Planet. Space Sci.* 113–114, 219–225.
- Encrenaz, P., et al., 2012a. HDO and SO<sub>2</sub> thermal mapping on Venus: evidence for strong SO<sub>2</sub> variability. *Astron. Astrophys.* 543.
- Encrenaz, T., Lellouch, E., Paubert, G., Gulkis, S., 1991. First detection of HDO in the atmosphere of Venus at radio wavelengths: an estimate of the H<sub>2</sub>O vertical distribution. *Astron. Astrophys.* 246, L63–L66.
- Encrenaz, T., Lellouch, E., Cernicharo, J., Paubert, G., Gulkis, S., Spilker, T., 1995. The thermal profile and water abundance in the Venus mesosphere from H<sub>2</sub>O and HDO millimeter observations. *Icarus* 117, 162–172.
- Encrenaz, T., et al., 2012b. HDO and SO<sub>2</sub> thermal mapping on Venus: evidence for strong SO<sub>2</sub> variability. *Astron. Astrophys.* 543 <https://doi.org/10.1051/0004-6361/201219419>.
- Encrenaz, T., et al., 2013. HDO and SO<sub>2</sub> thermal mapping on Venus. II. The SO<sub>2</sub> spatial distribution above and within the clouds. *Astron. Astrophys.* 559.

- Encrenaz, T., et al., 2016. HDO and SO<sub>2</sub> thermal mapping on Venus. *Astron. Astrophys.* 595, A74.
- Erard, S., et al., 2017. VESPA: a community-driven virtual observatory in planetary science. *Planet. Space Sci.* 150, 65–85.
- Fedorova, A., et al., 2008. HDO and H<sub>2</sub>O vertical distributions and isotopic ratio in the Venus mesosphere by solar occultation at infrared spectrometer onboard Venus Express. *J. Geophys. Res.* 113, E00B22.
- Fedorova, A., Marcq, E., Luginin, M., Korablev, O., Bertaux, J.-L., Montmessin, F., 2016. Variations of water vapor and cloud top altitude in the Venus' mesosphere from SPICAV/VEx observations. *Icarus* 275, 143–162.
- Gamache, R.R., Faresse, M., Renaud, C.L., 2016. A spectral line list for water isotopologues in the 1100–4100 cm<sup>-1</sup> region for application to CO<sub>2</sub>-rich planetary atmospheres. *J. Mol. Spectrosc.* 326, 144–150.
- Gurwell, M.A., Melnick, G.J., Tolls, V., Bergin, E.A., Patten, B.M., 2007. SWAS observations of water vapor in the Venus mesosphere. *Icarus* 188, 288–304.
- Hedin, A.E., Niemann, H.B., Kasprzak, W.T., 1983. Global empirical model of the Venus thermosphere. *J. Geophys. Res.* 88, 73–83.
- Krasnopolsky, V.A., 2012. A photochemical model for the Venus atmosphere at 47–112 km. *Icarus* 218, 230–246.
- Luginin, M., et al., 2016. Aerosol properties in the upper haze of Venus from SPICAV IR data. *Icarus* 277, 154–170.
- Luginin, M., Fedorova, A., Belyaev, D., Montmessin, F., Korablev, O., Bertaux, J.L., 2018. Scale heights and detached haze layers in the mesosphere of Venus from SPICAV IR data. *Icarus* 311, 87–104.
- Mahieux, A., et al., 2008. In-flight performance and calibration of SPICAV/SOIR on-board Venus Express. *Appl. Opt.* 47, 2252–2265.
- Mahieux, A., Wilquet, V., Drummond, R., Belyaev, D., Fedorova, A., Vandaele, A.C., 2009. A new method for determining the transfer function of an Acousto optical tunable filter. *Opt. Express* 17, 2005–2014.
- Mahieux, A., et al., 2010. Densities and temperatures in the Venus mesosphere and lower thermosphere retrieved from SOIR onboard Venus Express: retrieval technique. *J. Geophys. Res.* 115.
- Mahieux, A., et al., 2012. Densities and temperatures in the Venus mesosphere and lower thermosphere retrieved from SOIR on board Venus Express: carbon dioxide measurements at the Venus terminator. *J. Geophys. Res.* 117, E07001.
- Mahieux, A., et al., 2015a. Update of the Venus density and temperature profiles at high altitude measured by SOIR on board Venus Express. *Planet. Space Sci.* 113–114, 309–320.
- Mahieux, A., et al., 2015b. Venus mesospheric sulfur dioxide measurement retrieved from SOIR on board Venus Express. *Planet. Space Sci.* 113–114, 193–204.
- Mahieux, A., et al., 2015c. Rotational temperatures of Venus upper atmosphere as measured by SOIR on board Venus Express. *Planet. Space Sci.* 113–114, 347–358.
- Mahieux, A., Wilquet, V., Vandaele, A.C., Robert, S., Drummond, R., Bertaux, J.L., 2015d. Hydrogen halides measurements in the Venus upper atmosphere retrieved from SOIR on board Venus Express. *Planet. Space Sci.* 113–114, 264–274.
- Mahieux, A., Erwin, J., Vandaele, A.C., Wilquet, V., Yelle, R., 2020. A 1-D radiative transfer model of the Venus mesosphere and thermosphere: model description and comparison with SOIR/VEx. *Icarus*. In preparation.
- Marcq, E., et al., 2011. An investigation of the SO<sub>2</sub> content of the venusian mesosphere using SPICAV-UV in nadir mode. *Icarus* 211, 58–69.
- Marcq, E., Bertaux, J.L., Montmessin, F., Belyaev, D., 2013. Variations of sulphur dioxide at the cloud top of Venus's dynamic atmosphere. *Nat. Geosci.* 6, 25–28.
- Marcq, E., Mills, F.P., Parkinson, C.D., Vandaele, A.C., 2018. Composition and chemistry of the neutral atmosphere of Venus. *Space Sci. Rev.* 214, 10.
- Mills, F.P., 1999. Water vapor in the Venus middle atmosphere. *Adv. Space Res.* 23, 1573–1576.
- Mills, F.P., Esposito, L.W., Yung, Y.L., 2007. Atmospheric composition, chemistry and clouds. *Geophysical Monograph Series* 176, 73–100.
- Nevejans, D., et al., 2006. Compact high-resolution space-borne echelle grating spectrometer with AOTF based on order sorting for the infrared domain from 2.2 to 4.3 micrometer. *Appl. Opt.* 45, 5191–5206.
- Parkinson, C., Gao, P., Esposito, L., Yung, Y., Bougher, S.W., Hirtzig, M., 2015a. Photochemical control of the distribution of Venusian water. *Planet. Space Sci.* 113–114, 226–236.
- Parkinson, C., et al., 2015b. Distribution of sulphuric acid aerosols in the clouds and upper haze of Venus using Venus Express VAST and VeRa temperature profiles. *Planet. Space Sci.* 113–114, 205–218.
- Piccilli, A., Moreno, R., Encrenaz, T., Fouchet, T., Lellouch, E., Widemann, T., 2017. Mapping the thermal structure and minor species of Venus mesosphere with ALMA submillimeter observations. *Astron. Astrophys.* 606, A53 <https://doi.org/10.1051/0004-6361/201730923>.
- Régalia, L., Cousin, E., Gamache, R.R., Vispoel, B., Robert, S., Thomas, X., 2019. Laboratory measurements and calculations of line shape parameters of the H<sub>2</sub>O–CO<sub>2</sub> collision system. *J. Quant. Spectrosc. Radiat. Transf.* 231, 126–135.
- Rodgers, C.D., 2000. *Inverse Methods for Atmospheric Sounding: Theory and Practice*. University of Oxford.
- Rothman, L.S., et al., 2013. The HITRAN2012 molecular spectroscopic database. *J. Quant. Spectrosc. Radiat. Transf.* 130, 4.
- Sandor, B.J., Clancy, R.T., 2005. Water vapor variations in the Venus mesosphere from microwave spectra. *Icarus* 177, 129–143.
- Trompet, L., et al., 2016. Improved algorithm for the transmittance estimation of spectra obtained with SOIR/Venus Express. *Appl. Opt.* 55, 9275–9281.
- Trompet, L., et al., 2017. Description, accessibility and usage of SOIR/Venus Express atmospheric profiles of Venus distributed in VESPA (virtual European solar and planetary access). *Planet. Space Sci.* 150, 60–64.
- Vandaele, A.C., et al., 2008. Composition of the Venus mesosphere measured by SOIR on board Venus Express. *J. Geophys. Res.* 113, E00B23.
- Vandaele, A.C., et al., 2013. Improved calibration of SOIR/Venus Express spectra. *Opt. Express* 21, 21148.
- Vandaele, A.C., Mahieux, A., Robert, S., Drummond, R., Wilquet, V., Bertaux, J.L., 2015. Carbon monoxide short term variability observed on Venus with SOIR/VEX. *Planet. Space Sci.* 113–114, 237–255.
- Vandaele, A.C., et al., 2016a. Contribution from SOIR/VEX to the updated Venus International Reference Atmosphere (VIRA). *Adv. Space Res.* 57, 443–458.
- Vandaele, A.C., et al., 2016b. Carbon monoxide observed in Venus' atmosphere with SOIR/VEX. *Icarus* 272, 48–59.
- Vandaele, A.C., et al., 2017a. Sulfur dioxide in the Venus atmosphere: I. Vertical distribution and variability. *Icarus* 295, 16–33.
- Vandaele, A.C., et al., 2017b. Sulfur dioxide in the Venus atmosphere: II. Spatial and temporal variability. *Icarus* 295, 1–15.
- Wilquet, V., et al., 2009. Preliminary characterization of the upper haze by SPICAV/SOIR solar occultation in UV to mid-IR onboard Venus Express. *J. Geophys. Res.* 114, E00B42.
- Wilquet, V., Drummond, R., Mahieux, A., Robert, S., Vandaele, A.C., Bertaux, J.L., 2012. Optical extinction due to aerosols in the upper haze of Venus: four years of SOIR/VEX observations from 2006 to 2010. *Icarus* 217, 875–881.
- Zasova, L.V., Moroz, V.I., Linkin, V.M., Khatountsev, I.A., Maiorov, B.S., 2006. Structure of the Venusian atmosphere from surface up to 100 km. *Cosm. Res.* 44, 364–383.
- Zhang, X., Liang, M.C., Montmessin, F., Bertaux, J.L., Parkinson, C., Yung, Y.L., 2010. Photolysis of sulphuric acid as the source of Sulphur oxides in the mesosphere of Venus. *Nat. Geosci.* 3, 834–837.
- Zhang, X., Liang, M., Mills, F., Belyaev, D., Yung, Y., 2012. Sulfur chemistry in the middle atmosphere of Venus. *Icarus* 217, 714–739.